Sensors and Actuators Reports 8 (2024) 100255

Contents lists available at ScienceDirect

Sensors and Actuators Reports

journal homepage: www.sciencedirect.com/journal/sensors-and-actuators-reports

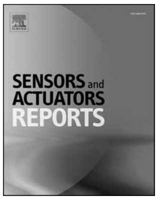

Enhancing nitrous oxide chemiresistive sensing performance by reducing ionic Oxygen species adsorption in Gold functionalized Tungsten Trioxide nanofibers

Dung Thi Hanh To, Bingxin Yang, Nosang Vincent Myung *

Department of Chemical and Biomolecular Engineering, University of Notre Dame, IN, 46628, USA

ARTICLE INFO

Keywords:
Nitrous oxide
Gold
Tungsten trioxide
Nanofibers
Chemiresistive sensor

ABSTRACT

Low-cost nitrous oxide (N_2O) gas sensor is in great need to provide real-time information to various stakeholders. Herein, various gold functionalized tungsten trioxide nanofibers (Au-WO_3 NFs) with different composition and crystallinity were synthesized by controlling electrospinning solutions and post heat treatment. These sensing materials were systematically exposed to various N_2O concentrations at different operating temperatures (*i.e.,* 250 to 450 °C). Among different samples, 1 at % gold functionalized WO_3 nanofibers (1 at % Au-WO_3 NF) annealed at 600 °C for 24 h shows the highest sensitivity ($S = R_a/R_o$) of 38.5 toward 100 ppm at 250 °C with experimentally determined limit of detection (LOD) at 2.5 ppm. Although recovery and recovery time improved, the sensitivity reduced with an increase in operating temperatures. The detailed sensing mechanism studies indicated that the high N_2O sensing was achieved when there were limited adsorbed ionized oxygen species (*e.g.,* O^-). Moreover, N_2O adsorption and desorption activation energy were estimated to be 0.13 and 0.87 eV where desorption was more strongly temperature dependent than adsorption.

1. Introduction

Nitrous oxide (N_2O) is a colorless gas with a lightly sweet odor which used as an anesthetic gas for medical purposes where used gas is released to the surroundings without further treatment. Thus, NIOSH set the permissible exposure limit (PEL) of 25 part per million (ppm) for a 10-hour time weighted average. N_2O is also a greenhouse gas with a lifespan of over 100 years and an environmental impact which is 25 times greater than CO_2 [1]. As a part of the nitrogen cycle, N_2O can be produced both naturally and anthropogenically from wastewater treatment and runoff and agricultural biomass [1]. N_2O is also used in electronics manufacturing, including semiconductors and liquid-crystal display. Further, it is utilized as a propellant and foaming agent in the food and beverage industry as well as a fuel oxidizer for rockets and racing cars [2,3]. Thus, the sensing performance needs to be optimized for different applications. For example, greenhouse gas emissions from natural and anthropogenic sources require the detection range in part per billion (ppb). On other hand, sensors for engineers and technicians working in semiconducting industries target a few ppm scales. To ensure the safety of workers and minimize climate change, high performance and low-cost N_2O gas sensors are critically needed to inform various stakeholders in a timely manner.

Among several types of gas sensors, chemiresistive sensor is one of most cost-effective sensors with high sensitivity, fast response and recovery times, and simple-signal acquisition process [1]. Although chemiresistive gas sensors are commercially available for many target analytes, there is no commercial N_2O chemiresistive gas sensor in the market due to difficulty in development of extremely sensitive sensor. Furthermore, limited works were reported in literature related to N_2O chemiresistive gas sensors [4]. In general, literature works showed that metal oxide functionalized with different dopants had higher sensitivity than pristine counterpart [5–8]. Kanazawa *et al.* systematically studied the doping effects on tin oxide (SnO_2) for N_2O detection. Compared to other metal oxides, SnO_2 showed the highest sensitivity ($S = R_a/R_o$) of 1.7 toward 300 ppm at 450 °C among 23 pristine metal oxides. Three noble metals and 21 oxides varying from p-type oxides to oxides of alkali, alkali earth, rare earth elements were then investigated as dopants. While all noble metals at 0.1 wt. % (*i.e.*, gold, palladium, rhodium) deteriorated sensitivity, metal oxides at 0.5 wt. % had suppression or facilitation on N_2O detection. 0.5 wt. % strontium oxide (SrO) increased N_2O sensitivity by three times at 500 °C with a trade-off of response and recovery time in compared to the pristine SnO_2. With effluent analysis

---

* Corresponding author.
E-mail address: nmyung@nd.edu (N.V. Myung).

https://doi.org/10.1016/j.snr.2024.100255
Received 27 July 2024; Received in revised form 2 September 2024; Accepted 30 October 2024

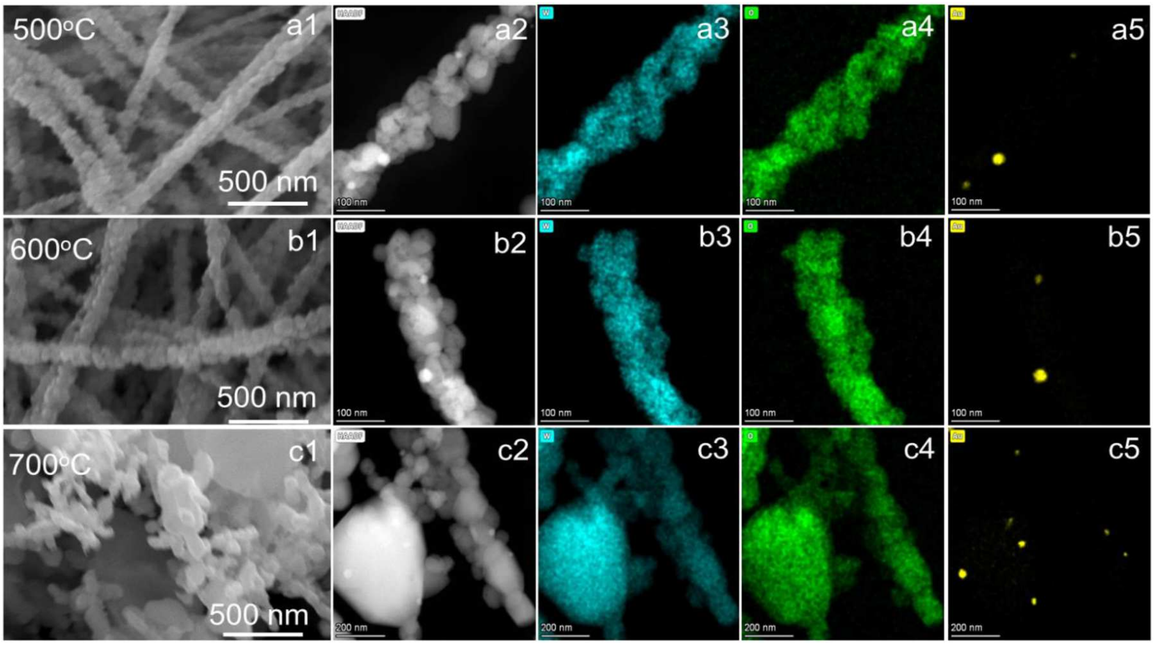

Fig. 1. SEM images (1), HAADF images (2), and EDS mapping of tungsten (3), oxygen (4), gold (5) of 1 at% Au-WO_3 NF annealed at 500 °C (a), 600 °C (b), and 700 °C (c).

by gas chromatography, the suppression of N_2O decomposition to form N_2 and O_2 was claimed to promote sensitivity for only certain metal oxides. Since the optimal temperature placed in the high end of testing temperature, absorbed oxygen species were suggested to have a predominant effect on sensitivity over the adsorbed N_2O [5,7]. Furthermore, Au nanoparticle decorated MoS_2 nano-flakes enhanced the sensitivity to 15.8 % in comparison to 10.5 % of pristine one towards 100 ppm N_2O at 22 °C [6]. Besides, one-dimensional structures exhibit higher sensitivity compared to macro and micro counterparts due to the greater surface area-to-volume ratio and the larger charge dispersion zone over cross-sectional area [8,9]. Rout et al. reported that reducing the diameter of In_2O_3 nanowires from 200 nm to 20 nm improved the sensitivity (R_a/R_o) from 9 to 60 toward 10 ppm N_2O and lowered the optimal temperature from 175 °C to 150 °C [10]. Although some sensing materials were reported for N_2O detection, the interests were falling in the scope of sensing performance, such as sensitivity and limit of detection. Most of the work lacks quantitative analysis of sensing mechanisms.

In our prior work, we demonstrated that sensing performance can be significantly improved by synthesizing inorganic and organic nanofibers with different composition, morphology, and crystallinity [11–16]. Unlike previous published work, this paper focuses on elucidating key parameters affecting sensing performance by exposing different gold functionalized WO_3 nanofibers (Au-WO_3 NF) to different concentrations of oxygen and N_2O at operating temperatures from 250 to 450 °C. Additionally, the effect of composition and crystallinity on sensing performance was systematically examined by fabricating WO_3 nanofibers with varying gold contents. Crystallinity and morphology were also altered by adjusting post-annealing temperature and time.

2. Experimental section

2.1. Nanofiber synthesis

Au-WO_3 NFs were synthesized via multi-needle electrospinning method, followed by a calcination process. 1.657 g of ammonium metatungstate hydrate ($(NH_4)_6H_2W_{12}O_{40}\cdot xH_2O$) and 0.8288 g of polyvinylpyrrolidone (M_W = 1300,000) were added into 12 ml of N,N-dimethylformamide (DMF) and stirred overnight to obtain homogenous precursor solution. Au-to-W atomic ratio varied from 1, 2, and 10 at % by adding different amounts of gold chloride trihydrate ($HAuCl_4\cdot 3H_2O$) into as-obtained homogenous precursor solutions. Precursor solution was then stirred until well mixed. Electrospinning was carried out with the setting of 13 kV voltage between needle and drum collector with a fixed flow rate of 0.25 mL/h. The temperature and relative humidity were also fixed at 40 °C and 12 %, respectively. All the chemicals were acquired from Sigma-Aldrich Co., Ltd., USA. Subsequently, as-spun nanofibers were calcinated in air at 500, 600, and 700 °C for 24 h to combust PVP, oxidize the tungsten precursor into tungsten oxide, and control the crystallinity.

2.2. Material characterization

X-ray diffraction (XRD, Rigaku MiniFlex 600) with parameters λ of 1.5406 Å was used in 2θ ranges from 20 to 70° with a step size of $2^\circ\cdot min^{-1}$ to determine crystal structure and average grain size. The morphology and nanofiber diameter were analyzed based on scanning electron microscopy (Prisma E SEM from Thermo Fisher Scientific, USA) images. High resolution transmission electron microscopy (HR-TEM) images and elemental mapping were acquired using Thermo Fisher Spectra 300. Ultra-Violet Visible (UV–Vis) reflectance spectra obtained using Ocean Optics DH-2000-BAL.

2.3. Sensor fabrication and sensing measurements

For gas sensors fabrication, as-synthesized nanofibers were dispersed in de-ionized water with a fixed concentration of 10 mg/mL and subsequently drop-casted on a microelectromechanical system (MEMS)-based micro hotplate with 10-micron gap gold interdigitated electrode (Maimaosi, China). Sensors were exposed to various gases (*i.e.*, N_2, air, N_2O) concentration and operating temperatures (250–450 °C). The electrical resistance values of each gas sensing material were determined and acquired using a voltage divider method using ten bits analog digital converter (ADC) in Arduino Mega 2560. Gas sensing response is defined as $S = R_a/R_o$, where R_a refers to resistance under analyte and R_o indicates resistance in carrier gas. Adsorbed oxygen species were determined by varying the operating temperatures in the presence of different oxygen concentrations with nitrogen as a carrier gas. Details of procedure are

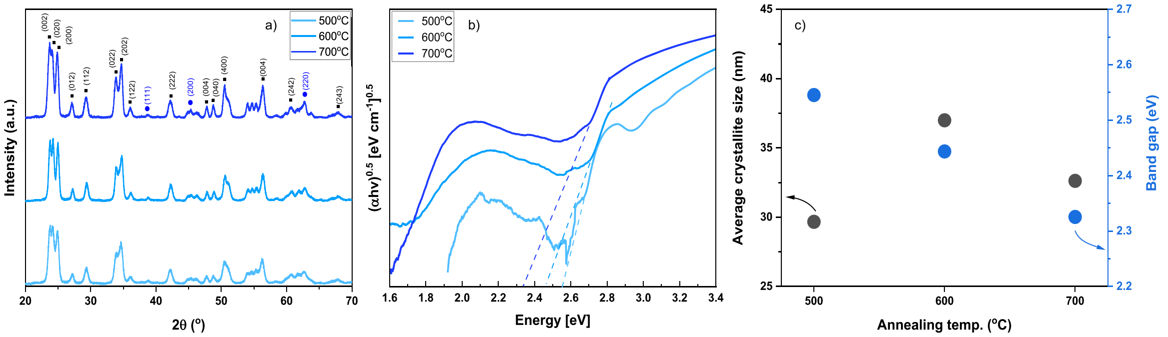

Fig. 2. XRD patterns (a) and Tau plot (b) of 1 at % Au-WO_3 NF at different annealing temperatures. Calculated average grain size and band gap (c) as a function of annealing temperature.

available in previous works [17,18]. The measured resistance was then plotted against the partial pressure of oxygen in a natural logarithmic plot following the Eq. (1). The slope or the n value is then employed to determine the adsorbed oxygen species. In addition, the potential energy barrier (E_b) was determined by the plot of measured resistance *versus* operating temperature as in Eq. (2) **.

$$R = aP^n \ or\ or\ lnR = c + nlnP \tag{1}$$

[19]

$$R(T) = R_o \exp\left(\frac{E_b}{k_B T}\right) or\ lnR(T) = lnR_o + \frac{E_b}{k_B T} \tag{2}$$

[20]

Where P is partial pressure of oxygen, a,n,c are constant, Ro is a preexponential factor with the dimension of a resistance, k_B is Boltzmann constant. T is the operating temperature in Kelvin unit.

3. Result and discussion

3.1. Material characterization and gas sensing performance

3.1.1. Effects of annealing temperatures

After electrospinning and thermal treatment in air to remove polymer, morphology and elemental distribution of gold functionalized WO_3 were characterized using SEM and HR-TEM (Fig. 1**)**. As shown in the figure**,** increasing annealing temperatures from 500 to 600 °C results in no notable change of nanofibers morphology whose diameters are around 65 ± 17 nm. However, the nanofibers which were thermally treated at 700 °C caused a loss of one-dimensional structure and formation of nano and microparticle mixture. This might be because of the fast-burning rate of polymer and/or organic residue at 700 °C causing the collapse of one-dimensional structure. [21] HAADF images show that nanofibers consist of smaller grains aligning in one-dimensional structures. Also, EDS mapping indicates the uniform distribution of W and O atoms, while Au nanoparticles form on nanofiber surfaces with smaller size than WO_3 grains.

XRD patterns show the presence of monoclinic WO_3 (JCPDS # 83–0951) and cubic Au (JCPDS # 04–0784) whose peaks are marked in

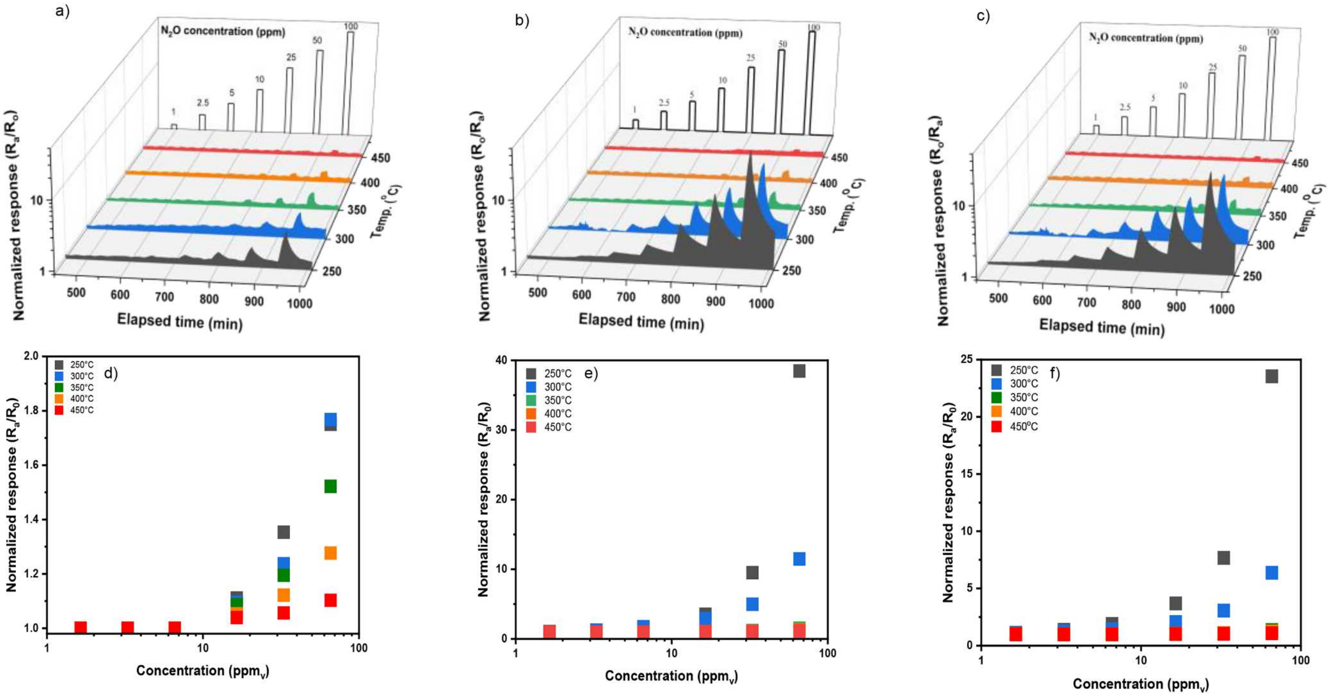

Fig. 3. Annealing temperature dependent real-time sensing response (a-c) and normalized response (d-f) toward different N_2O concentration at various operating temperatures. 500 (a,d), 600 (b,e), and 700 °C (c,f). Gold content was fixed at 1 at % for all samples.

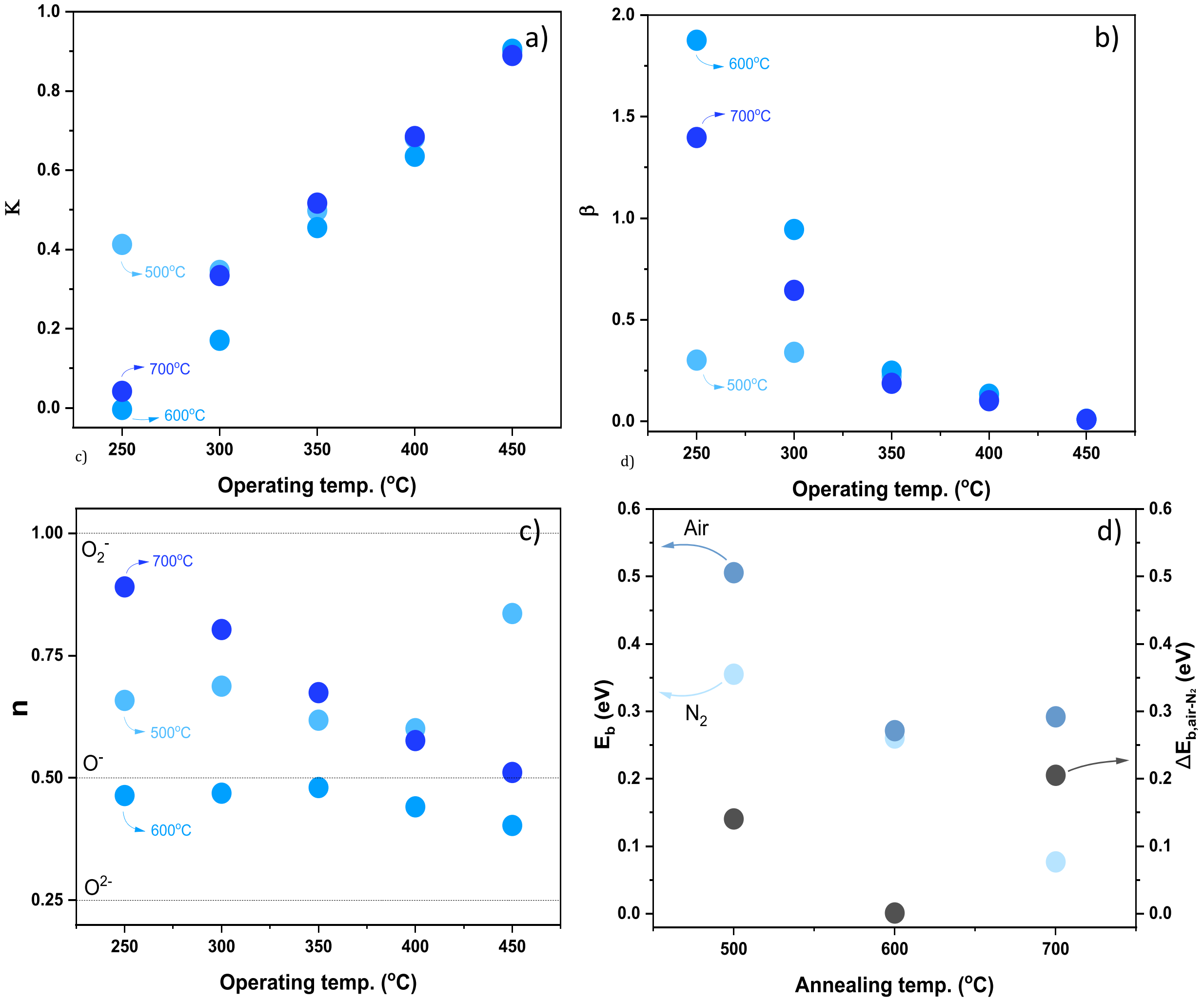

Fig. 4. Annealing temperature dependent K (a) and β (b) toward N_2O, and n (c) as a function of operating temperature. Potential energy barrier (E_b) in N_2, air and the difference (ΔE_b) between them (d) as a function of annealing temperature. 1 at % Au-WO_3 NF were annealed at 500, 600, and 700 °C.

black square and blue circle respectively (Fig. 2). [18,22,23] Moreover, the peak shape becomes sharper at higher annealing temperatures due to grain growth. Peak shifts of 0.05° to the larger 2Θ and of 0.04° to smaller 2Θ in comparison to 500 °C sample were observed for 600 °C and 700 °C samples respectively as in **Fig. S1**. This indicates the unit cell of WO_3 gets smaller at 600 °C and larger at 700 °C. The non-monotonic change of unit cell with increasing temperature might be ascribed to the loss of morphology at elevated temperature of 700 °C. In other words, more gold atoms might be trapped in the WO_3 lattice structure at 700 °C when the polymer and organic residue are burnt quickly, and the 1-D structure collapses. By using the Scherrer equation, average grain sizes are calculated to be in the range of 25–40 nm (Fig. 2**c**). Since grain growth is expected with an increase in annealing temperature, a larger grain size is observed at 600 °C. However, this trend does not occur at 700 °C, and the grain becomes smaller than that of sample annealed at 600 °C. This observation might be attributed to more gold atoms which act as impurity at the grain boundary and suppress grain migration of WO_3. [22,24,25] In contrast, the materials become more electrically conductive with narrower band gaps with higher annealing temperature. As shown in Fig. 2**c**, the band gaps which reduce from 2.55 to 2.33 eV, are consistent with reported values for noble metal functionalized WO_3. [18,26,27]

Fig. 3 shows the real-time normalized sensor response upon exposure to different concentrations of N_2O (*i.e.,* 1 to 100 ppm) at five different operating temperatures (*i.e.,* 250, 300, 350, 400, and 450 °C). Among different nanofibers, 1at. % Au-WO_3 NF annealed at 600 °C shows the highest sensitivity at 250 °C with the detection limit as low as 2.5 ppm. Lower operating temperatures lead to higher sensitivity and lower detection limit but slower recovery. Moreover, signal saturation occurs at higher operating temperatures. These findings are consistent for all nanofibers annealed at different temperatures. The optimal temperature in the lower range was also observed for other one-dimensional metal oxides. [10]

The sensing responses as shown in Fig. 3**d-f** were also extracted from normalized resistance at the end of the analyte exposure and fitted using power law in Eq. (3) to obtain K and β constants to understand the sensing mechanism at different operating temperatures [17,19]. K is determined by the operating conditions and sensing materials, and β is derived from the interaction between analytes and adsorbed oxygen or sensing materials [19]. While β reaches the maximum values at the optimal temperatures, K becomes the minimum as shown in Fig. 4**a-b**. Also, higher annealing temperatures shifts the optimal temperatures to smaller values. In other words, 300 °C leads to the highest sensitivity for nanofibers annealed at 500 °C, but the samples annealed at 600 and 700 °C are the most sensitive at 250 °C. Nonetheless, the variation of K and β among three samples became indifferent at 350 °C or higher, implying that adsorption/desorption of N_2O became less dependent on material properties and morphology at higher operating temperatures. On the other hand, this is consistent with the changes of oxygen ionic species with operating temperatures in Fig. 4**c-d**. The adsorbed oxygen species

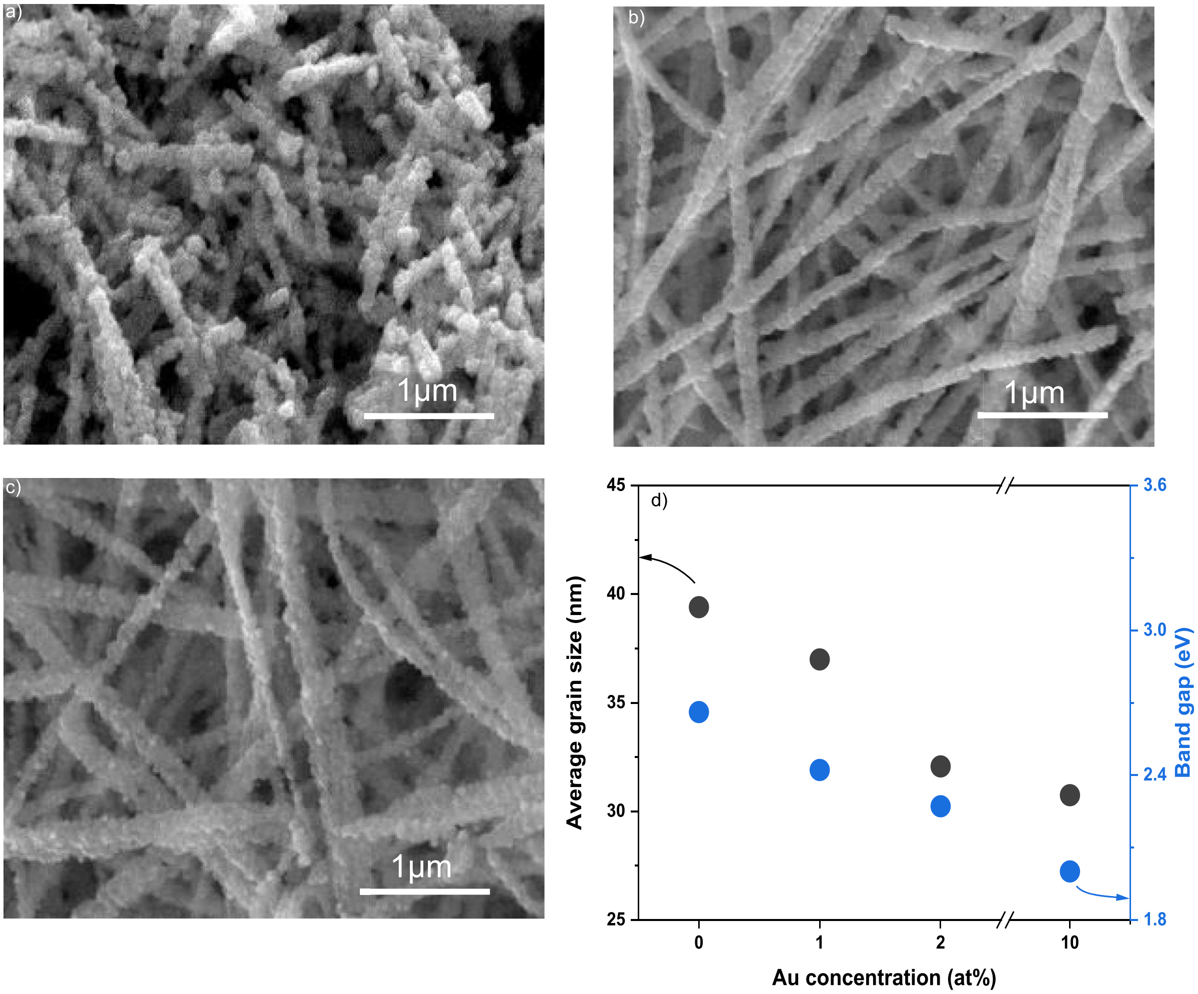

Fig. 5. SEM images of pristine (a), 2 (b), and 10 (c) at.% Au-WO_3 NF. Calculated average grain size and band gap (d) as a function of Au content. All Au-WO_3 NF were annealed at 600 °C.

at different temperatures are estimated by the slope (*n* value) of sensor resistance at different oxygen concentrations. *n* values of 1, 0.5, 0.25 correspond to the presence of O_2^-, O^- and O^{2-} respectively, and values in between suggest mixtures of species. [19,28] In general, the *n* values decrease at higher operating temperatures, implying that adsorbed oxygen species have higher valence states or more charges are transferred between sensing materials and oxygen as shown in equations 4–6 [8,29,30]. Fig. 4**c** shows that 1 at % Au-WO_3 NF annealed at 500 °C and 700 °C have mixtures of $O_2^-$and O^- whereas O^- is predominant for the sample at 600 °C. To quantify the effects of oxygen adsorption on potential energy barriers, E_b in N_2 ($E_{b,N2}$) and air ($E_{b,air}$) as well as the difference between them (ΔE_b) were calculated and correlated in Fig. 4**d**. Higher annealing temperatures cause lower $E_{b,N2}$ which is attributed to the lower band gap. The smallest E_b in the presence of air and ΔE_b are observed at the annealing temperature of 600 °C. The smaller ΔE_b corresponds to the smaller amount of adsorbed oxygen or smaller amount of electron withdrawn from sensing material. The depletion layer is thereby thinner, resulting in a smaller potential energy barrier. The smaller amount of adsorbed oxygen species might come from the smaller number of active sites for oxygen adsorption and/or surface charge carriers (electrons) available to transfer to adsorbed oxygen. Since both oxygen and N_2O withdraw electrons from sensing materials, the highest sensitivity from sample annealed at 600 °C suggests that surface charge carrier might not be the main reason for the smallest E_b and ΔE_b. In other words, oxygen and N_2O adsorption requires distinct types of active sites, and the number of active sites for oxygen adsorption is smallest on the sample with highest N_2O sensitivity. Moreover, larger grain size, which results in fewer grain boundary and thereby depletion layer, corresponds to lower E_b upon exposure to air for different annealing temperatures as shown in Fig. 2c & 4d. The N_2O sensitivity would be enhanced with smaller grain size and more and less active sites for N_2O and O_2 respectively theoretically. However, the Au functionalized WO_3 with highest sensitivity towards N_2O corresponds to the largest grain size and least number of active sites for oxygen, indicating the grain size has less effects of the sensing performance.

$$\text{Sensing response (S)} = \frac{R_a}{R_o} = K \times [N_2O]^{\beta} \tag{3}$$

where R_a is the electrical resistance of sensor upon exposure to analyte or N_2O, R_o is the electrical resistance of sensor upon exposure to dry air (baseline), $[N_2O]$ is the concentration of N_2O.

$$O_{2,gas} + e^- \leftrightarrow O_2^-{}_{ads} \tag{4}$$

$$O_{2,gas} + 2e^- \leftrightarrow 2O^-{}_{ads} \tag{5}$$

$$O_{2,gas} + 2e^- \leftrightarrow O_{ads}^{-2} \tag{6}$$

3.1.2. Effects of gold content

Since thermally treated 1 at % Au-WO_3 NF at 600 °C showed a better sensing performance, Au-WO_3 NF with different gold contents were synthesized and thermally treated at the same temperature. Following

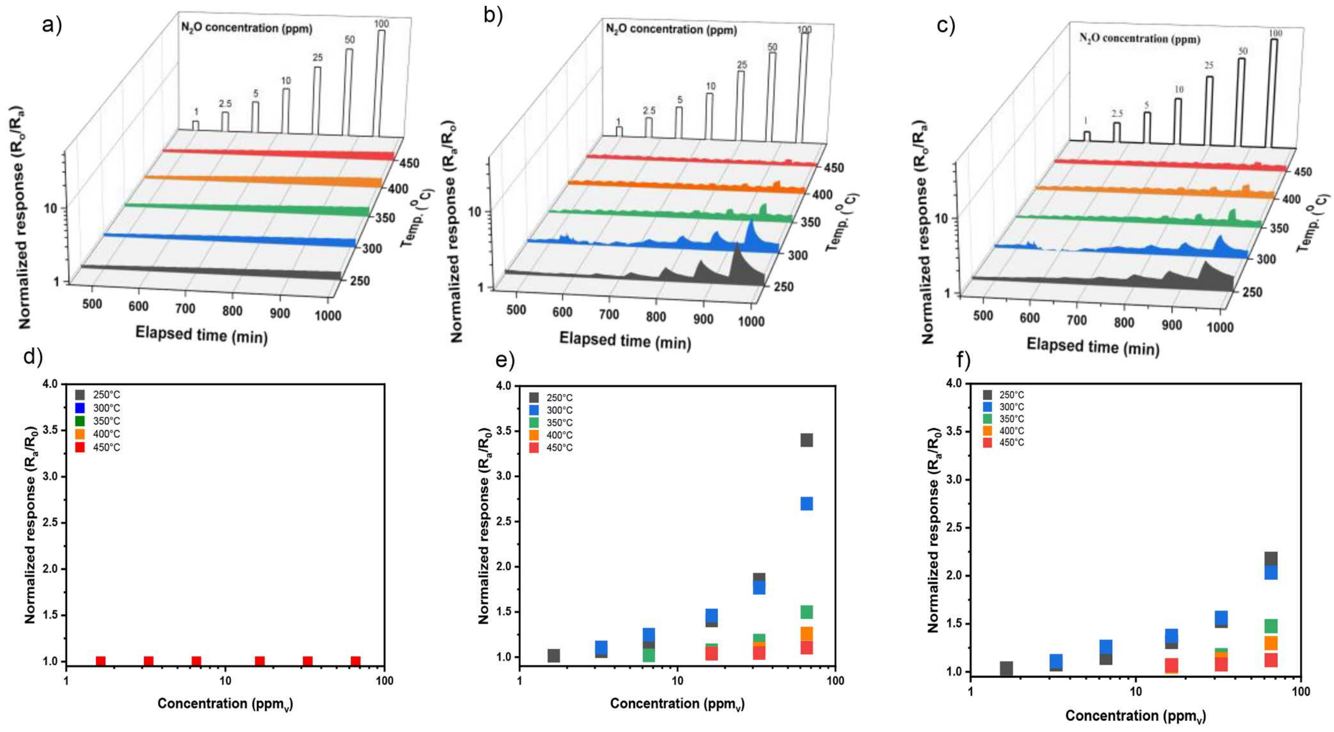

Fig. 6. Gold content dependent real-time sensing response (a-c) and normalized response (d-f) toward different N_2O concentrations at various operating temperatures (250 to 450 °C): Pristine (a,d), 2 (b,e), and 10 at % (c,e) Au-WO_3 NF. All samples were annealed at 600 °C for 24 h.

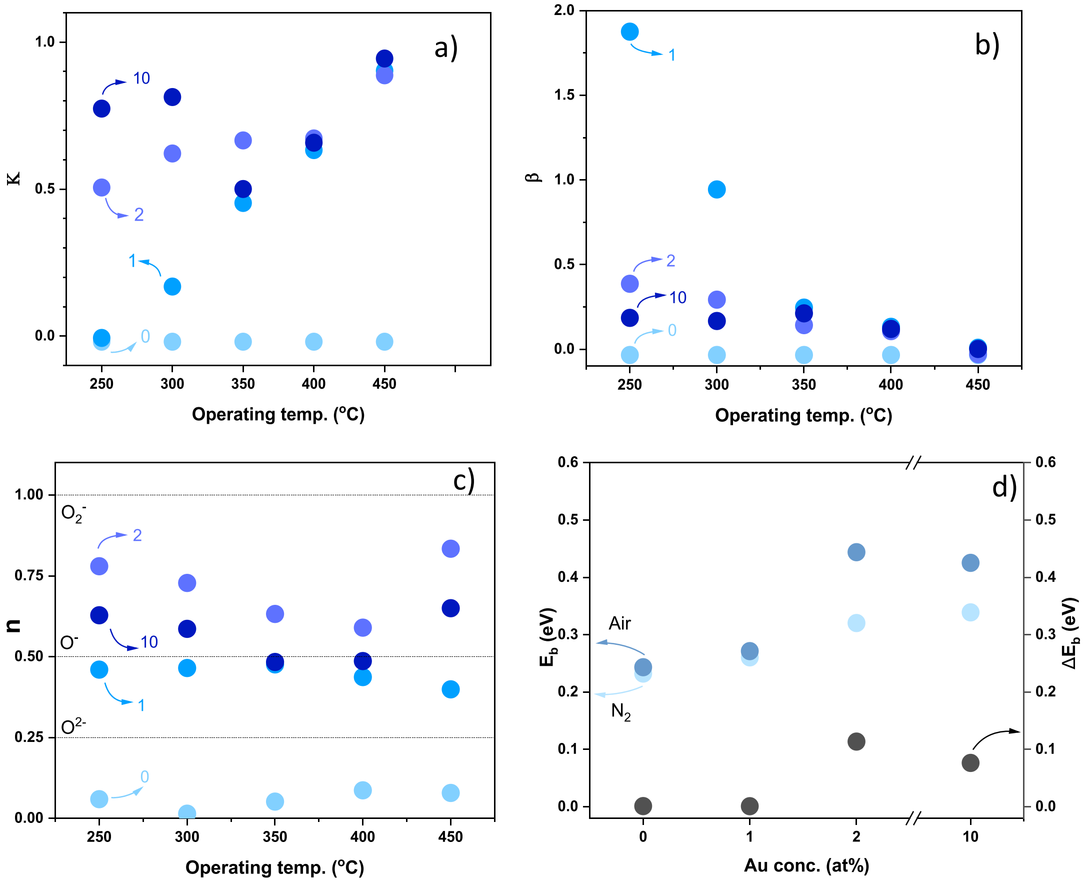

Fig. 7. Gold content dependent K (a) and β (b) toward N_2O, and n (c) as a function of operating temperature. Potential energy barrier in N_2, air and the difference (ΔE_b) between them (d) of Au-WO_3 NF. All samples were annealed at 600 °C.

the same procedure, material characterization of WO_3 functionalized with different gold content was conducted. SEM images in Fig. 5**a-c** show insignificant differences in nanofiber diameter, while the length became shorter without gold. XRD patterns in **Fig. S2a** also confirm the monoclinic and cubic structures of WO_3 (JCPDS # 83–0951) and Au (JCPDS # 04–0784) respectively. Gold peaks labeled in blue become more pronounced at higher gold content. Moreover, increasing gold content reduces grain size and band gap as shown in Fig. 5**d**. The smaller grain size might be caused by the grain boundary pinning effect of gold atoms [22,24,25]. Functionalized with gold also introduces an intermediate energy level between the valence and conduction band of the WO_3, resulting in smaller band gaps at higher gold contents [31,32]. Tauc plot of Au-WO_3 NF with different gold content is available in the Supplemental Information (**Fig. S2b**).

Gold content has effects on material properties and thereby sensing performance as shown in Fig. 6. The optimal gold content is found at 1 at % above which the sensitivity towards N_2O is lower, and pristine WO_3 showed no response. Rahman et al. also reported an optimal Au content of 25 nM in the range of 0–200 nM for Au nanoparticle decorated MoS_2 without further study of Au content effects [6]. Kanazawa et al. reported that 0.1 wt.% noble metal (*e.g.*, Au, Pd, Rh) doped SnO_2 deteriorated N_2O sensing, suggesting noble metal content plays a critical role in N_2O sensing performance [5]. Operating temperature has a similar effect on different gold content in comparison to samples annealed at different temperatures. All samples reach their highest sensitivity at 250 °C. Although 1 at % Au-WO_3 NF sample has higher sensitivity than 2 and 10 at % Au sample at lower operating temperatures, no significant difference is observed at 350 °C and higher. This finding is also seen when fitted K and β values are correlated with operating temperatures in Fig. 7**a-b**. K and β have similar values at higher temperatures (*i.e.*, 350 °C and above). Furthermore, increasing gold content reduces the variation of K and β with operating temperatures, implying that higher Au content does not directly affect N_2O oxidation.

The attempts to deconvolute the Au content effect was conducted by determining the adsorbed oxygen species and the potential energy barrier caused by them. In Fig. 7**c**, ionic oxygen species with higher valence states or smaller *n* values are formed at lower gold contents. O^{2-} and O^- ions are predominantly formed on pristine WO_3 NF and 1 at % Au-WO_3 NF respectively. On the other hand, mixtures of O_2^- and O^- form on 2 and 10 at % Au-WO_3 NF. Among four samples, the effects of oxygen adsorption on potential energy barriers are higher at higher Au contents (2 and 10 at %) while insignificant impacts are found at 0 and 1 at % content as shown in Fig. 7**d**. This implies that gold might facilitate or catalyze the oxygen adsorption and dissociation and thereby higher fraction of adsorbed oxygen species on surface of sensing materials [33,34]. On the other hand, higher valence state adsorbed oxygen species were formed at 0 and 1 at % Au with less active sites for adsorption. This finding explains the observed effect of gold contents on adsorbed oxygen species and ΔE_b. A higher fraction of surface area occupied by the absorbed oxygen species might lead to smaller absorbed N_2O and lower sensitivity. This is consistent with the small variation of K and β with operating temperatures at higher gold contents. The correlation between sensing performance and E_b, ΔE_b of pristine WO_3 and 1at. % Au-WO_3 NF suggests a significant role of gold content on N_2O detection. Furthermore, N_2O sensing experiments in N_2 carrier gas were conducted for 1at % and 10at% Au-WO_3 NF to understand the effects of Au content. As shown in Fig. S3, N_2O sensitivity in N_2 environment is higher than that in air environment for the 10 at % while no significant enhancement in sensitivity is observed for the 1 at% Au-WO_3. In both environments, 1 at % Au-WO_3 shows higher sensitivity toward N_2O. Using the single crystalline monoclinic WO_3 nanowires, Rout et al. reported a sensitivity of 24 for 100 ppm N_2O at 250 °C. [10] This indicates that crystallinity or defects control the competition between oxygen and N_2O adsorption besides gold content. Further study is required to understand the mechanism of such a low gold content as 1 at.%.

Table 1
N_2O sensing performance of different metal oxides.

Sens. mat.	Mor.	N_2O conc. (ppm)	Oper. temp. (°C)	Sensitivity	LOD (ppm) *	Carrier gas	Ref.
WO_3	–	300	450	1.30	–	Air	[7]
ZnO	–			1.20	–		
In_2O_3	–			1.10	–		
SnO_2	–			1.70	–		
0.5 wt% SrO-SnO_2	–			4.50			
SnO_2		100	500	1.10	–	Air	[5]
0.5 wt% SrO-SnO_2	–	100	500	2.40	–		
0.5 wt% Bi_2O_3-SnO_2	–	100	500	1.60	–		
0.5 wt% CaO-SnO_2	–	100	500	1.70	–		
0.5 wt% Sm_2O_3-SnO_2	–	100	500	1.80	35		
SnO_2	Thin film	100	210	11.5	10	Air	[35]
In_2O_3	200 nm-NW	100	150	12.5	0.1	Air	[10]
In_2O_3	20 nm-NW	100	150	80.0	0.1		
WO_3	200 nm-NW	100	250	24.0	0.1		
MoS_2	Flake-like	100	22	1.10	–	N_2	[6]
Au-MoS_2	Flake-like	100	22	1.16	10		
H-plasma SnO_2	Thin film	100	RT	1.55	–	Air	[36]
Au-WO_3 NF	NF	100	250	38.5	2.5	Air	This work

* Experimentally determined: Sensitivity = R_a/R_o.

Among six samples, 1 at % Au-WO_3 NF annealed at 600 °C has the highest sensitivity of 38.5 toward 100 ppm N_2O at 250 °C. This sample also shows good selectivity over different analytes, including ammonia, methane, carbon monoxide, and hydrogen, at the concentration of 50 ppm and 250 °C as shown in **Fig. S3** 1 at % Au-WO_3 NF has low sensitivity towards CO and no response to CH_4. On the other hand, responses of three were observed for NH_3 and H_2. Besides selectivity, the reproducibility of this sample in Fig. S4 shows negligible change at lower tested concentration and small reduction at higher concentration range. Before investigating the sensing mechanism of this Au-WO_3 NF, the performance of 6 samples was compared with other literature works as shown in Table 1. Au-WO_3 NF in this work is in the higher end of sensitivity range and lower end of operating temperature range in comparison with other reported works. The discussion has focused on studying the effects of annealing temperature and gold content on the sensing performance by correlating material properties with K, β, oxygen adsorption species, and potential energy barrier. Besides thermodynamics, kinetics is investigated for the best sample (*i.e.*, 1 at % Au-WO_3 NF annealed at 600 °C) to explain its performance.

3.1.3. *Gas sensing mechanisms*

Adsorbed oxygen is generally accepted to have a key role in metal oxide-based chemiresistive gas sensors. As an oxidizing gas, N_2O molecules compete with oxygen molecules for electrons from the conduction band of sensing materials as shown in equations 5a, 7 [5,33,37]. As adsorbed oxygen species are determined to be O^- predominantly, equation 5a is considered for oxygen adsorption only.

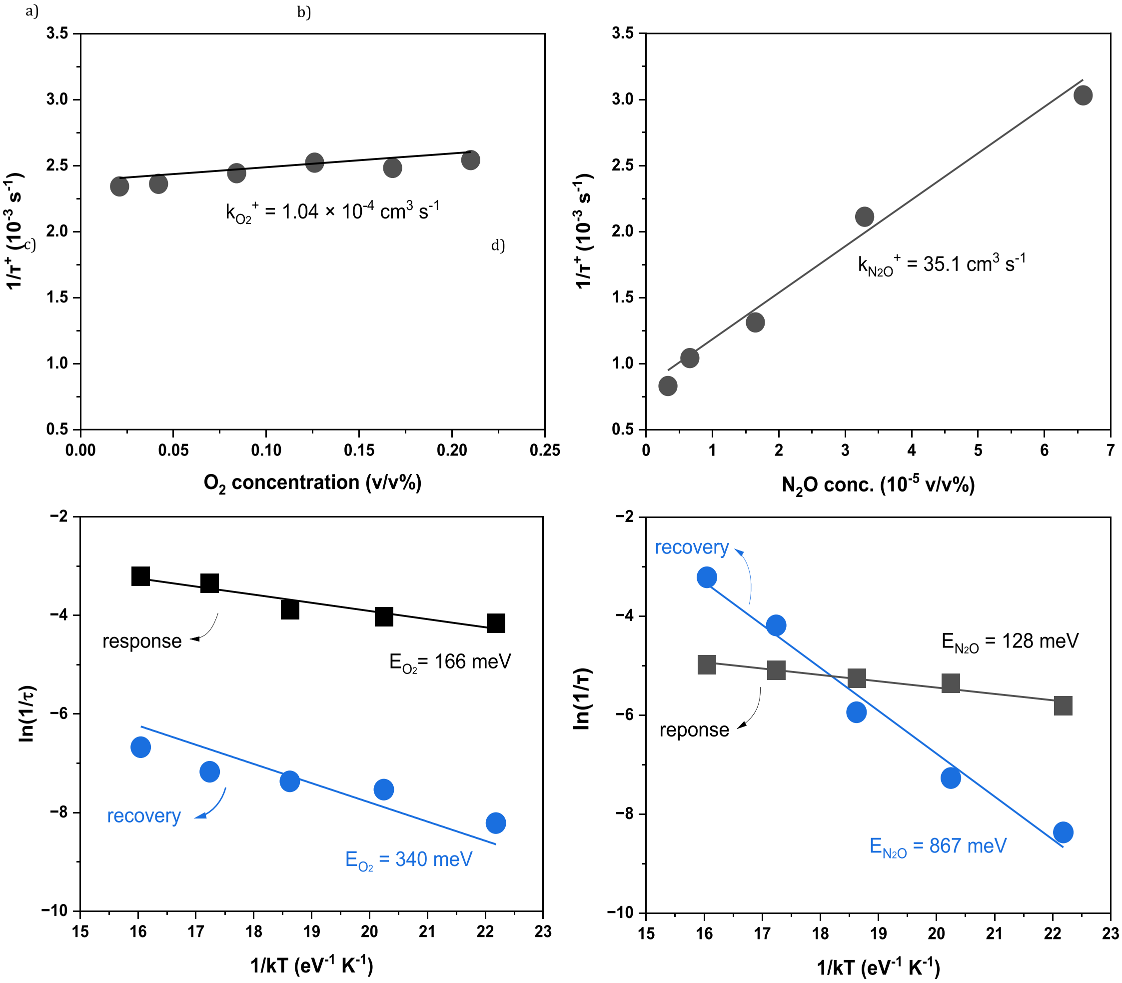

Fig. 8. Adsorption rate constant of O_2 (a) and N_2O (b) at operating temperature of 250 °C. Activation energy for adsorption/desorption of O_2 (c) and N_2O (d) of 1at% Au-WO_3 NF annealed at 600 °C.

$$O_{2,\mathrm{gas}} + 2e^- \overset{k_1^+}{\underset{k_1^-}{\leftrightarrow}} 2O^-_{\mathrm{ads}} \tag{5a}$$

$$N_2O_{\mathrm{gas}} + e^- \overset{k_2^+}{\underset{k_2^-}{\leftrightarrow}} N_{2,\mathrm{gas}} + O^-_{\mathrm{ads}} \tag{7}$$

To correlate the receptor (adsorption/desorption kinetics) and transduction (resistance/conductance changes) functions of materials, Langmuir adsorption model is utilized to determine rate constants from gas sensing performance. Fitting changes of resistance over time (data not shown) indicates that analyte adsorption follows first-order reaction process which is used to derive the relationship between oxygen-occupied sites, reaction rate constants and conductance. The details of derivation are discussed in the work by Vuong *et al.* [38] The competition between N_2O and O_2 is deconvoluted by studying the adsorption and desorption of oxygen in N_2 as carrier gas and those of N_2O in air subsequently. Before exposure to analytes (*i.e.*, oxygen and N_2O), sensors were purged with carrier gases to achieve stable resistance. In other words, the adsorption of carrier gases reaches their equilibrium, and any changes in resistance upon analyte exposures come from analyte adsorption. Considering $N_i(t)$ as the analyte-occupied sites at time t (i = 1 and 2 for oxygen and N_2O respectively), the rates of change of $N_i(t)$ in the response and recovery cycles are as shown in Eqs. (8) and (9) respectively.

$$\frac{dN_i(t)}{dt} = k_i^+[N - N_i(t)]C_i + k_i^- N_i(t) \tag{8}$$

$$\frac{dN_i(t)}{dt} = -k_i^- N_i(t) \tag{9}$$

Where k_i^+ *and* k_i^- represent adsorption and desorption rate constant of analyte i whereas C_i represent the concentration of analyte *i.*

Eqs. (8) and (9) can be solved to an exponential decay curve and then combined with Poisson's equation for conductance of nanowire to obtain time-dependent conductance change ($\Delta G(t)$) in response and recovery cycles as shown in Eqs. (10) and (11) respectively. [38] Adsorption and desorption time constants, which can be achieved by fitting the conductance changes over time, are used to determine adsorption and desorption rate constants via Eqs. (12) and (13). Details on conversion between conductance and resistance and plots of conductance change over time are in Supplemental Information and **Fig. S6–7**.

$$\Delta G(t) = \Delta G_{\max}\left[1 - \exp\left(-\frac{t}{\tau_i^+}\right)\right] \tag{10}$$

$$\Delta G(t) = \Delta G_{max}\exp\left(-\frac{t}{\tau_i^-}\right) \tag{11}$$

$$\tau_1^+ = \frac{1}{k_i^+ C_i + k_i^-} \tag{12}$$

$$\tau_i^- = \frac{1}{k_i^-} \tag{13}$$

where $\Delta G(t) = G(0) - \mathrm{G(t)}$

$\Delta G_{max} = \mathrm{G(0)} - \mathrm{G_{max}}$

τ_i^+, τ_i^- : adsorption and desorption time constants of analyte i

G(0) and G_{max}: conductance at time 0 and highest conductance of response/recovery cycle of interest

After determining the adsorption and desorption time constants, the adsorption rate constants were determined by linear fitting $1/\tau$ *vs* oxygen concentration as shown in Fig. 8**a-b**. As shown, N_2O has a much higher adsorption affinity than O_2 toward Au-WO_3 NF at 250 °C. Moreover, the desorption rate constant of N_2O is about 10^5 times lower than adsorption rate constant, which explains the long recovery time. Besides rate constant, activation energy for adsorption and desorption was determined by linear fitting the natural log of $1/\tau$ and 1/kT. 20 % v/v O_2 in N_2 (*i.e.*, air) and 100 ppm were selected to study the temperature effects. As shown in Fig. 8**c-d**, activation energy for adsorption of N_2O is smaller than that of O_2. As expected, the activation energy for desorption is larger than that for adsorption. Moreover, the desorption activation energy of N_2O is significantly larger and more temperature-dependent than that of O_2. Increasing temperature from 250 to 450 °C, the time constant reduces about 3 times as in Fig. 8**d**. This is consistent with changes of resistance in the response and recovery cycles in Fig. 3**b**.

4. Conclusion

Gold functionalized WO_3 nanofibers with varied gold content (0–10 at%) were electrospun and sequentially post-thermal treated at different temperatures (500–700 °C). All fibers have similar diameters. Polycrystalline gold functionalized WO_3 consists of cubic Au and monoclinic WO_3 with grain size <50 nm. Nanofibers with smaller band gaps were observed at higher annealing temperatures and higher gold concentration. The nanofibers were employed as sensing materials for N_2O detection at different operating temperatures. Sweet spots for both synthesis parameters were observed at 1 at % Au and 600 °C, which resulted in highest sensitivity of 38.5 at 100 ppm N_2O and limit of detection of 2.5 ppm. Optimal operating temperature for most samples occurs at 250 °C. Using power law fitting to correlate the sensing performance and analyte concentration, smallest K and largest β occur at optimal temperature. Moreover, K and β of samples with different annealing temperatures are more operating temperature dependent than those of different Au contents. Analyses of adsorbed oxygen species and potential energy barriers imply that oxygen and N_2O adsorption occur on different active sites. Moreover, gold acts as catalyst for oxygen adsorption and dissociation and thereby suppressing N_2O interaction with sensing materials. While most samples form a mixture of O_2^- and O^- with more active sites, 1 at % Au-WO_3 NF annealed at 600 °C has fewer active sites for predominant formation of O^-. The best sample for N_2O detection has 10^5 times more affinity to N_2O than O_2. Furthermore, activation energy for N_2O adsorption is smaller than that for O_2. In contrast, activation energy for O_2 desorption is lower and less temperature-dependent than that for N_2O. This work highlights that morphology and crystallinity need to be optimized with noble metal content to maximize the sensing performance.

CRediT authorship contribution statement

Dung Thi Hanh To: Writing – original draft, Formal analysis, Data curation. **Bingxin Yang:** Methodology, Investigation, Data curation. **Nosang Vincent Myung:** Writing – review & editing, Project administration, Funding acquisition, Conceptualization.

Declaration of competing interest

The authors declare that they have no known competing financial interests or personal relationships that could have appeared to influence the work reported in this paper.

Acknowlegement

This work was partially funded by the NSF ITE #2344028. The authors appreciate Dr. Maksym Zhukovsky for his knowledge and expertise for TEM analysis at Notre Dame Integrated Imaging Facility United States.

Supplementary materials

Supplementary material associated with this article can be found, in the online version, at doi:10.1016/j.snr.2024.100255.

Data availability

Data will be made available on request.

References

[1] J. Milam-Guerrero, B. Yang, D.T. To, N.V. Myung, Nitrous Oxide Is No Laughing Matter: a Historical Review of Nitrous Oxide Gas-Sensing Capabilities Highlighting the Need for Further Exploration, ACS. Sens. 7 (12) (2022) 3598–3610, https://doi.org/10.1021/acssensors.2c01275.

[2] D. Razus, Nitrous Oxide: oxidizer and Promoter of Hydrogen and Hydrocarbon Combustion, Ind. Eng. Chem. Res. 61 (31) (2022) 11329–11346, https://doi.org/10.1021/acs.iecr.2c01774.

[3] V. Zakirov, M. Sweeting, T. Lawrence, J. Sellers, Nitrous oxide as a rocket propellant, Acta Astronaut. 48 (5) (2001) 353–362, https://doi.org/10.1016/S0094-5765(01)00047-9.

[4] K. Wetchakun, T. Samerjai, N. Tamaekong, C. Liewhiran, C. Siriwong, V. Kruefu, A. Wisitsoraat, A. Tuantranont, S. Phanichphant, Semiconducting metal oxides as sensors for environmentally hazardous gases, Sens. Actuators B 160 (1) (2011) 580–591, https://doi.org/10.1016/j.snb.2011.08.032.

[5] E. Kanazawa, G. Sakai, K. Shimanoe, Y. Kanmura, Y. Teraoka, N. Miura, N. Yamazoe, Metal oxide semiconductor N2O sensor for medical use, Sens. Actuators B 77 (1) (2001) 72–77, https://doi.org/10.1016/S0925-4005(01)00675-X.

[6] M.T. Rahman, R.R. Khan, Y. Tian, H. Ibrahim, L. Dong, High-Sensitivity and Room-Temperature Nitrous Oxide Sensor Using Au Nanoparticles-Decorated MoS2, IEEE Sens. J. 23 (17) (2023) 18994–19001, https://doi.org/10.1109/JSEN.2023.3296504.

[7] E. Kanazawa, G. Sakai, K. Shimanoe, Y. Kanmura, Y. Teraoka, N. Miura, N. Yamazoe, Semiconductor Gas Sensor Using SrO - Modified SnO2 for the Detection of N 2 O in Air, Electrochem. Solid-State Lett. 3 (12) (2000) 572, https://doi.org/10.1149/1.1391212.

[8] B. Yang, N.V. Myung, T. Tran, T. 1D Metal Oxide Semiconductor Materials for Chemiresistive Gas Sensors: a Review, Adv. Electron. Mater. 7 (9) (2021) 2100271, https://doi.org/10.1002/aelm.202100271, 10.1002/aelm.202100271(acccessed 2022/12/30).

[9] T. Zhang, S. Mubeen, N.V. Myung, M.A. Deshusses, Recent progress in carbon nanotube-based gas sensors, Nanotechnology. 19 (33) (2008) 332001, https://doi.org/10.1088/0957-4484/19/33/332001.

[10] C.S. Rout, K. Ganesh, A. Govindaraj, C.N.R. Rao, Sensors for the nitrogen oxides, NO_2, NO and N_2O, based on In_2O_3 and WO_3 nanowires, Appl. Phys. A 85 (3) (2006) 241–246, https://doi.org/10.1007/s00339-006-3707-9.

[11] B.X. Yang, D.T.H. To, E.R. Mendoza, N.V. Myung, Achieving One Part Per Billion Hydrogen Sulfide (H2S) Level Detection through Optimizing Composition and Crystallinity of Gold-Decorated Tungsten Trioxide (Au-WO_3)) Nanofibers, ACS. Sens. 9 (1) (2024) 292–304, https://doi.org/10.1021/acssensors.3c01979.

[12] B. Yang, T.-T. Tran, J. Milam-Guerrero, D.T. To, T. Stahovich, N.V. Myung, Enhancing gas sensing performance of tungsten trioxide (WO3) nanofibers through diameter and crystallinity control, Sens. Actuator Rep. 7 (2024) 100182, https://doi.org/10.1016/j.snr.2023.100182.

[13] B. Yang, D. Thi Hanh To, D. Sobolak, E.R. Mendoza, N.V. Myung, High performance methyl salicylate gas sensor based on noble metal (Au, Pt) decorated WO3 nanofibers, Sens. Actuators B 413 (2024) 135741, https://doi.org/10.1016/j.snb.2024.135741.

[14] K. Low, C.B. Horner, C.L. Li, G. Ico, W. Bosze, N.V. Myung, J. Nam, Composition-dependent sensing mechanism of electrospun conductive polymer composite nanofibers, Sens. Actuat. B 207 (2015) 235–242, https://doi.org/10.1016/j.snb.2014.09.121.

[15] C.L. Li, N. Chartuprayoon, W. Bosze, K. Low, K.H. Lee, J. Nam, N.V. Myung, Electrospun Polyaniline/Poly(ethylene oxide) Composite Nanofibers Based Gas Sensor, Electroanal 26 (4) (2014) 711–722, https://doi.org/10.1002/elan.201300641.

[16] H. Park, H. Jung, M.L. Zhang, C.H. Chang, N.G. Ndifor-Angwafor, Y. Choa, N. V. Myung, Branched tellurium hollow nanofibers by galvanic displacement

reaction and their sensing performance toward nitrogen dioxide, Nanoscale 5 (7) (2013) 3058–3062, https://doi.org/10.1039/c3nr00060e.

[17] D.T.H. To, J.Y. Park, B. Yang, N.V. Myung, Y.-H. Choa, Nanocrystalline ZnO quantum dot-based chemiresistive gas sensors: improving sensing performance towards NO2 and H2S by optimizing operating temperature, Sens. Actuators. Rep. 6 (2023) 100166, https://doi.org/10.1016/j.snr.2023.100166.

[18] B. Yang, D.T.H. To, E. Resendiz Mendoza, N.V. Myung, Achieving One Part Per Billion Hydrogen Sulfide (H2S) Level Detection through Optimizing Composition and Crystallinity of Gold-Decorated Tungsten Trioxide (Au-WO3) Nanofibers, ACS. Sens. (2024), https://doi.org/10.1021/acssensors.3c01979.

[19] Z. Hua, Y. Li, Y. Zeng, Y. Wu, A theoretical investigation of the power-law response of metal oxide semiconductor gas sensors I: schottky barrier control, Sens. Actuators B 255 (2018) 1911–1919, https://doi.org/10.1016/j.snb.2017.08.206.

[20] A. Ponzoni, Metal Oxide Chemiresistors: A Structural and Functional Comparison Between Nanowires and Nanoparticles, Sensors, 2022, p. 22.

[21] Y. Pan, Y. Liu, G. Zeng, L. Zhao, Z. Lai, Rapid synthesis of zeolitic imidazolate framework-8 (ZIF-8) nanocrystals in an aqueous system, Chem. Commun. 47 (7) (2011) 2071–2073, https://doi.org/10.1039/C0CC05002D, 10.1039/C0CC05002D.

[22] P. Jaroenapibal, P. Boonma, N. Saksilaporn, M. Horprathum, V. Amornkitbamrung, N. Triroj, Improved NO2 sensing performance of electrospun WO3 nanofibers with silver doping, Sens. Actuators B 255 (2018) 1831–1840, https://doi.org/10.1016/j.snb.2017.08.199.

[23] S.R. Vijayan, P. Santhiyagu, M. Singamuthu, N. Kumari Ahila, R. Jayaraman, K. Ethiraj, Synthesis and Characterization of Silver and Gold Nanoparticles Using Aqueous Extract of Seaweed, *Turbinaria conoides,*and Their Antimicrofouling Activity, Sci. World J. (2014) 938272, https://doi.org/10.1155/2014/938272, 2014.

[24] S.-W. Tsai, J.-C. Chiou, Improved crystalline structure and H2S sensing performance of CuO–Au–SnO2 thin film using SiO2 additive concentration, Sens. Actuators B. 152 (2) (2011) 176–182, https://doi.org/10.1016/j.snb.2010.12.004.

[25] D.-J. Yang, I. Kamienchick, D.Y. Youn, A. Rothschild, I.-D. Kim, Ultrasensitive and Highly Selective Gas Sensors Based on Electrospun SnO2 Nanofibers Modified by Pd Loading, Adv. Funct. Mater. 20 (24) (2010) 4258–4264, https://doi.org/10.1002/adfm.201001251 (acccessed 2024/01/27).

[26] S. Pari, N.S. Jha, T.S. Ganesan, S.K. Jha, Pulse Electrodeposited Au–WO3 Catalyst from a Water–Ionic Liquid Microemulsion for Photoaccelerated Methanol Electrooxidation, J. Phys. Chem. 124 (40) (2020) 21957–21967, https://doi.org/10.1021/acs.jpcc.0c05656.

[27] T. Anh Thu Do, D.T. Nguyen, T.G. Ho, H.T. Giang, Q.N. Pham, T. Ha Lien Nghiem, T.H. Nguyen, M.T Man, Enhanced catalytic activity of WO3–Au nanotubes: mechanism and environmental remediation potential, J. Mater. Sci. 34 (35) (2023) 2246, https://doi.org/10.1007/s10854-023-11631-z.

[28] Z. Hua, C. Tian, D. Huang, W. Yuan, C. Zhang, X. Tian, M. Wang, E. Li, Power-law response of metal oxide semiconductor gas sensors to oxygen in presence of reducing gases, Sens. Actuators B 267 (2018) 510–518, https://doi.org/10.1016/j.snb.2018.04.002.

[29] A. Staerz, U. Weimar, N. Barsan, Current state of knowledge on the metal oxide based gas sensing mechanism, Sens. Actuators B 358 (2022) 131531, https://doi.org/10.1016/j.snb.2022.131531.

[30] H. Ji, W. Zeng, Y. Li, Gas sensing mechanisms of metal oxide semiconductors: a focus review, Nanoscale 11 (47) (2019) 22664–22684, https://doi.org/10.1039/C9NR07699A, 10.1039/C9NR07699A.

[31] S. Kumar, V. Singh, A. Tanwar, Structural, morphological, optical and photocatalytic properties of Ag-doped ZnO nanoparticles, J. Mater. Sci 27 (2) (2016) 2166–2173, https://doi.org/10.1007/s10854-015-4227-1.

[32] R. Chen, C. Zou, J. Bian, A. Sandhu, W. Gao, Microstructure and optical properties of Ag-doped ZnO nanostructures prepared by a wet oxidation doping process, Nanotechnology. 22 (10) (2011) 105706, https://doi.org/10.1088/0957-4484/22/10/105706.

[33] D. Degler, S. Rank, S. Müller, H.W. Pereira de Carvalho, J.-D. Grunwaldt, U. Weimar, N Barsan, Gold-Loaded Tin Dioxide Gas Sensing Materials: mechanistic Insights and the Role of Gold Dispersion, ACS. Sens. 1 (11) (2016) 1322–1329, https://doi.org/10.1021/acssensors.6b00477.

[34] M. Hübner, D. Koziej, J.-D. Grunwaldt, U. Weimar, N. Barsan, An Au clusters related spill-over sensitization mechanism in SnO2-based gas sensors identified by operando HERFD-XAS, work function changes, DC resistance and catalytic conversion studies, Phys. Chem. Chem. Phys. 14 (38) (2012) 13249–13254, https://doi.org/10.1039/C2CP41349C, 10.1039/C2CP41349C.

[35] J. Lančok, A. Santoni, M. Penza, S. Loreti, I. Menicucci, C. Minarini, M. Jelinek, Tin oxide thin films prepared by laser-assisted metal–organic CVD: structural and gas sensing properties, Surf. Coat. Technol. 200 (1) (2005) 1057–1060, https://doi.org/10.1016/j.surfcoat.2005.02.131.

[36] A. Chaturvedi, V.N. Mishra, R. Dwivedi, S.K. Srivastava, Selectivity and sensitivity studies on plasma treated thick film tin oxide gas sensors, Microelectronics. J. 31 (4) (2000) 283–290, https://doi.org/10.1016/S0026-2692(99)00147-0.

[37] N.B. Wong, Y.B. Taarit, J.H. Lunsford, Formation of O− in ZnO from the dissociation of adsorbed N2O, J. Chem. Phys. 60 (5) (2003) 2148–2151, https://doi.org/10.1063/1.1681325 (acccessed 1/10/2024).

[38] N.M. Vuong, D. Kim, H. Kim, Surface gas sensing kinetics of a WO3 nanowire sensor: part 1—Oxidizing gases, Sens. and Actuators B: Chemical 220 (2015) 932–941, https://doi.org/10.1016/j.snb.2015.06.031.